

Possible Evidence of a Universal Radio/X-ray Correlation in a near-Complete Sample of Hard X-ray Selected Seyfert Galaxies

N. Chang^{1,2*}, F. G. Xie^{3*}, X. Liu^{1,4*}, L. C. Ho^{5,6}, A.-J. Dong^{1,7}, Z. H. Han⁸, X. Wang^{1,2}

¹ Xinjiang Astronomical Observatory, Chinese Academy of Sciences, 150 Science 1-Street, Urumqi 830011, Xinjiang, China

² School of Astronomy and Space Science, University of Chinese Academy of Sciences, Beijing, 100049, China

³ Key Laboratory for Research in Galaxies and Cosmology, Shanghai Astronomical Observatory, Chinese Academy of Sciences, 80 Nandan Road, Shanghai 200030, China

⁴ Key Laboratory of Radio Astronomy, Chinese Academy of Sciences, Nanjing 210008, China

⁵ Kavli Institute for Astronomy and Astrophysics, Peking University, Beijing 100871, China

⁶ Department of Astronomy, School of Physics, Peking University, Beijing 100871, China

⁷ Guizhou Provincial Key Laboratory of Radio Astronomy and Data Processing, Guizhou Normal University, Guiyang 550001, China

⁸ Physics and Electronic Engineering Department, Xinjiang Normal University, Urumqi 830000, China

Accepted XXX. Received YYY; in original form ZZZ

ABSTRACT

Because the disc–jet coupling likely depends on various properties of sources probed, the sample control is always an important but challenging task. In this work, we re-analyzed the *INTEGRAL* hard X-ray-selected sample of Seyfert galaxies. We only consider sources that have measurements in black hole mass, and luminosities in radio and X-rays. Our final sample includes 64 (out of the original 79) sources, consists of both bright AGNs and low-luminosity ones. The 2–10 keV X-ray Eddington ratio L_X/L_{Edd} locates in the range between $\sim 10^{-4.5}$ and $\sim 10^{-0.5}$. We first find that, because of the similarity in the L_{HX}/L_X distribution, the X-ray origin of radio-loud Seyferts may be the same to that of radio-quiet ones, where we attribute to the hot accretion flow (or similarly, the corona). We then investigate the connections between luminosities in radio and X-rays. Since our sample suffers a selection bias of a black hole mass M_{BH} dependence on L_X/L_{Edd} , we focus on the correlation slope ξ_X between the radio (at 1.4 GHz) and X-ray luminosities in Eddington unit, i.e. $(L_R/L_{\text{Edd}}) \propto (L_X/L_{\text{Edd}})^{\xi_X}$. We classify the sources according to various properties, i.e. 1) Seyfert classification, 2) radio loudness, and 3) radio morphology. We find that, despite these differences in classification, all the sources in our sample are consistent with a universal correlation slope ξ_X (note that the normalization may be different), with $\xi_X = 0.77 \pm 0.10$. This is unexpected, considering various possible radio emitters in radio-quiet systems. For the jet (either relativistic and well collimated, or sub-relativistic and weakly collimated) interpretation, our result may suggest a common/universal but to be identified jet launching mechanism among all the Seyfert galaxies, while properties like black hole spin and magnetic field strength only play secondary roles. We further estimate the jet production efficiency η_{jet} of Seyfert galaxies, which is $\eta_{\text{jet}} \approx 1.9^{+0.9}_{-1.5} \times 10^{-4}$ on average. We also find that η_{jet} increases as the system goes fainter. Alternative scenarios for the radio emission in radio-quiet systems are also discussed.

Key words: galaxies: active – galaxies: Seyfert – radio continuum: galaxies – accretion: accretion discs

1 INTRODUCTION

Almost every galaxy contains a supermassive black hole (BH) at its center (Kormendy & Ho 2013). Among most of the cosmic time the BH remains quiet; only over a short period of $10^4 - 10^6$ yrs (e.g., Kauffmann & Haehnelt 2000; Martini & Weinberg 2001; Condon et al. 2013), the BH is fed with a sufficient amount of gas/material and the system becomes active and luminous, i.e. enter a phase so-called the active galactic nucleus (AGN). It is now widely accepted that the AGN and its host galaxy are tightly connected, i.e. the host galaxy provides the feed for the accretion, while the energy and momentum driven by the AGN will also impact the dynamics

of the gas (consequently, the star formation) within the galaxy (for reviews, see e.g., Fabian 2012; Kormendy & Ho 2013; Heckman & Best 2014).

The structure of AGN is admittedly complex. Emission at different wavebands may originate from different physical components or different spatial locations (see e.g., Ho 2008; Heckman & Best 2014 for reviews), i.e. continuum radiation in radio, optical-ultraviolet (UV), and hard X-rays originates from, respectively, the relativistic jet, the cold accretion disc and the corona (or hot accretion flow in case of low-luminosity AGNs, here we use them interchangeably). The highly collimated jet, which propagates from sub-pc up to Mpc scales, may play a crucial role in the BH-host galaxy co-evolution (e.g., Croton et al. 2006; Heckman & Best 2014), although it remains inclusive on its basic physics, e.g., its composition and the launching and acceleration/deceleration mechanisms (see e.g., Harris &

* E-mail: changning@xao.ac.cn (NC), fgxie@shao.ac.cn (FGX), liux@xao.ac.cn (XL)

Krawczynski 2006; Tchekhovskoy 2015; Davis & Tchekhovskoy 2020 for summaries, and Parfrey, Philippov & Cerutti 2019; Chen & Zhang 2020 for recent progress). Statistically, as the systems become fainter, the fraction of radio-loud AGNs increases (Ho 2008), which agrees with observations in black hole binaries (Fender et al. 2009). Observationally jets in AGNs are diverse in both power and morphology (Padovani 2016; Panessa et al. 2019; Chiaraluce et al. 2020). Depending on the radio-to-optical luminosity ratio, the AGNs can be separated into two main classes. The minorities are radio-loud (RL), where the jet is highly relativistic and well collimated (for reviews, see e.g., Harris & Krawczynski 2006; Blandford, Meier, & Readhead 2019; Hardcastle & Croston 2020). Based on their large-scale radio morphology, the RL AGNs can be further classified to FR I or II (Fanaroff & Riley 1974). The rest majorities are radio-quiet (RQ), where the radio emission is compact, without clear well-collimated structure in high-resolution observations. The origin of the radio emission in RQ AGNs is still under debate, a significant fraction of the large-scale radio emission may originate from stellar processes, or from interactions between AGN wind and interstellar medium (e.g., Condon 1992; Padovani et al. 2015; Panessa et al. 2019; Chiaraluce et al. 2020). Even for the compact radio core (of RQ systems) investigated in this work, the origin is still inclusive, either a weak jet adopted here, or nuclear activities related to star formation (e.g., Laor & Behar 2008; Bonchi et al. 2013; Baek et al. 2019; Smith et al. 2020). Under the jet interpretation, the jet velocity is low (e.g., non-relativistic) and the collimation of jet is poor. Despite these observational differences, it is argued that jet among these systems may be governed by the same physics (Chen & Zhang 2020).

For the investigation of the connection of the jet and the accretion flow (more clearly, the hot accretion flow. See Yuan & Narayan 2014 for a review) in AGNs and BH X-ray binaries (BHBs), a tight linear relationship in logarithmic space among the BH mass M_{BH} , and the radio (monochromatic, $L_{\text{R}} = \nu L_{\nu}$ at e.g. 1.4 GHz) and X-ray (integrated, i.e. $L_{\text{X}} = \int L_{\nu} d\nu$ in e.g. the 2–10 keV band) luminosities has been discovered (e.g., Merloni et al. 2003; Falcke et al. 2004; Panessa et al. 2007; Li, Wu & Wang 2008; Gültekin et al. 2009, 2019; Burlon et al. 2013; Liu et al. 2016; Inoue et al. 2017; Qian et al. 2018). It is also called the “fundamental plane” (FP) of BH activity.¹ Motivated by accretion theory (see this suggestion in Xie & Yuan 2017), we consider the FP in a revised space, i.e. $(\log(L_{\text{R}}/L_{\text{Edd}}), \log(L_{\text{X}}/L_{\text{Edd}}), \log M_{\text{BH}})$ and re-express it as,

$$\log(L_{\text{R}}/L_{\text{Edd}}) = \xi_{\text{X}} \log(L_{\text{X}}/L_{\text{Edd}}) + \xi_{\text{M}} \log M_{\text{BH}} + \text{const.} \quad (1)$$

Here $L_{\text{Edd}} = 1.26 \times 10^{46} (M_{\text{BH}}/10^8 M_{\odot}) \text{ erg s}^{-1}$ is the Eddington luminosity. $L_{\text{R}}/L_{\text{Edd}}$ and $L_{\text{X}}/L_{\text{Edd}}$ define the Eddington ratios in radio and X-rays, respectively. We focus on the dependence on the luminosity (i.e. slope parameter ξ_{X}), but not on the BH mass (i.e. ξ_{M}). It is found that a majority of sources follow a “standard” $\xi_{\text{X}} \approx 0.6 \pm 0.1$ FP (see e.g., Merloni et al. 2003; Gültekin et al. 2009, 2019; Qian et al. 2018, and for the case of BHBs only, see e.g., Corbel et al. 2003, 2013). Studies suggest that the FP exist only in less luminous (e.g., sub-Eddington, see Merloni & Heinz 2008) systems. Theoretically the FP can be naturally interpreted under the framework of an accretion–jet model (e.g., Heinz & Sunyaev

2003; Yuan, Cui & Narayan 2005; Xie & Yuan 2016), where a hot accretion flow co-exists with a relativistic or mildly relativistic jet.² Observationally, individual sources may have a large scatter to the FP. Such scatter can be due to effects of, among others, the (combination of) BH spin (Miller et al. 2009; Ünal & Loeb 2020), the strength of the magnetic field (Blandford & Znajek 1977; Sikora et al. 2007; Li & Xie 2017), the Doppler beaming effect (Li, Wu & Wang 2008), and the environment (van Velzen & Falcke 2013).

Ever since its discovery, deviations to the standard FP in ξ_{X} are observed in different classes of systems, e.g., the radio-loud AGNs (e.g., Wang, Wu & Kong 2006; Panessa et al. 2007; Li, Wu & Wang 2008; de Gasperin et al. 2011), and the narrow-line Seyfert 1 galaxies (e.g., Yao et al. 2018). Such deviation is also observed in BHBs (e.g., Coriat et al. 2011; Corbel et al. 2013; Xie, Yan & Wu 2020). It is thus clear that ξ_{X} depends on the sample compilation, and its value may hint on the accretion mode of individual (type) of sources (e.g., Heinz & Sunyaev 2003; Xie & Yuan 2016; Xie, Yan & Wu 2020). Indeed, theoretically we can link the radio and X-ray luminosities to the dimensionless mass accretion rate \dot{m}^3 as (see e.g., Ünal & Loeb 2020)

$$L_{\text{R}}/L_{\text{Edd}} \propto \dot{m}^{\gamma}, \quad \text{and} \quad L_{\text{X}}/L_{\text{Edd}} \propto \dot{m}^{\kappa}, \quad (2)$$

where $\gamma \approx 1.3 - 1.4$ (e.g., Heinz & Sunyaev 2003). In the above expressions, additional dependence on, e.g., magnetic field strength and BH spin, is omitted for simplicity. Parameters γ and κ characterize respectively, the radiative efficiencies of jet and hot accretion flow, i.e. $L_{\text{R}}/(\dot{M}c^2) \propto \dot{m}^{\gamma-1}$ and $L_{\text{X}}/(\dot{M}c^2) \propto \dot{m}^{\kappa-1}$. Physically the observation of ξ_{X} then measures the value of $\gamma/\kappa \approx (1.3 - 1.4)/\kappa$. If we additionally estimate the jet power as $P_{\text{jet}} \propto L_{\text{R}}^{6/7}$ (Willott et al. 1999; Cavagnolo et al. 2010; Su et al. 2017), then the FP also provides information on the connection between powers in accretion and ejection, which can then used to probe the efficiency of converting accretion power into ejection (e.g., Inoue et al. 2017; Rusinek et al. 2020; Soares & Nemmen 2020; Wójtowicz et al. 2020).

With the advantage of free from absorption, the $\gtrsim 10$ keV hard X-rays provide a more direct measurement of the accretion power (especially of the hot accretion flow, which tightly correlates with jet). An unbiased hard X-ray selected sample, e.g., the *INTEGRAL*/*IBIS* selected sample of Panessa et al. 2015 (hereafter P15; see Section 2.1), will then be of great importance in the disc–jet coupling investigation. Most sources in the P15 Seyfert sample have $L_{\text{X}}/L_{\text{Edd}} \gtrsim 10^{-3}$, i.e. they belong to bright AGNs, and only a limited number of sources belong to low-luminosity ones ($L_{\text{X}}/L_{\text{Edd}} \lesssim 10^{-3}$). It is known that bright AGNs and low-luminosity ones are distinctive in their accretion physics (Ho 2008; Heckman & Best 2014). Theoretically bright AGNs are powered by cold accretion disk (e.g., Shakura–Sunyaev disc [SSD], Shakura & Sunyaev 1973), while low-luminosity AGNs are powered by hot accretion flow (Yuan & Narayan 2014).

P15 focused on correlations among luminosities of their absolute values (e.g., L_{R} and L_{X}), but not the Eddington normalized ones (e.g., $L_{\text{R}}/L_{\text{Edd}}$ and $L_{\text{X}}/L_{\text{Edd}}$), thus differences in accretion physics are

¹ Note that there are at least two types of jets, one is continuous/steady and the other is transient/episodic shown as discrete blobs, see e.g., Fender et al. (2009) for the classification of these two types of jets in BHBs. There may also exist a third type of jet (e.g., Xie, Yan & Wu 2020; Zdziarski et al. 2020 and references therein). In the FP studies only the continuous/steady jets are considered.

² As stated above, the origin of radio emission in RQ AGNs is questioned in recent years (e.g., Bonchi et al. 2013; Baek et al. 2019; Smith et al. 2020, see Panessa et al. 2019 for a review), where they argue the contributions from nuclear star formation, outflow, corona and jet are of comparable importance in many RQ AGNs.

³ Dimensionless accretion rate \dot{m} is defined as $\dot{m} = \dot{M}/\dot{M}_{\text{Edd}}$, i.e. the mass accretion rate \dot{M} normalized by the Eddington accretion rate $\dot{M}_{\text{Edd}} = 10 L_{\text{Edd}}/c^2$.

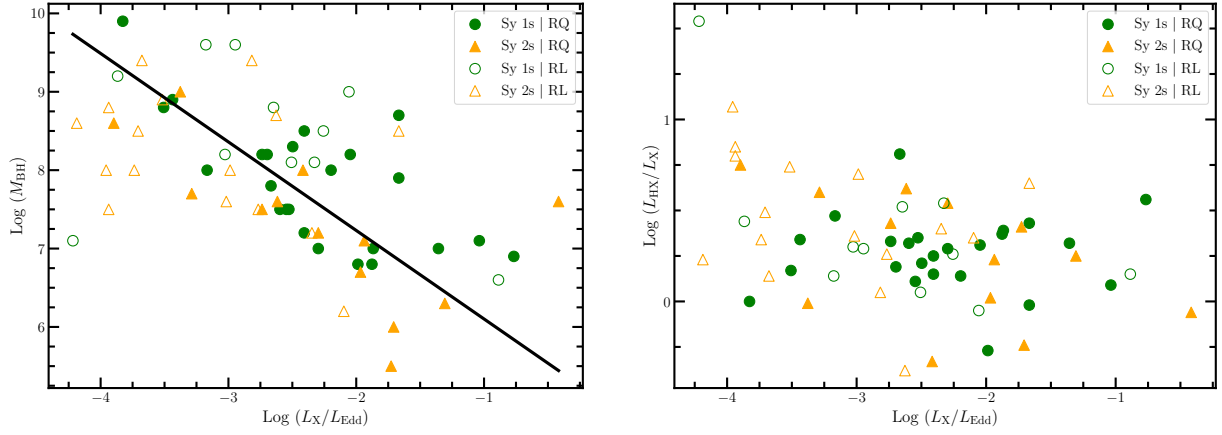


Figure 1. Distributions of BH mass M_{BH} (left panel) and the 20-100 keV to 2-10 keV X-ray flux ratio $L_{\text{HX}}/L_{\text{X}}$ (right panel) versus 2-10 keV X-ray Eddington ratio $L_{\text{X}}/L_{\text{Edd}}$. In both panels, the open and filled separate sources in their radio loudness, i.e. open for radio-loud (RL) and filled for radio-quiet (RQ); while the color and shape define their optical properties, i.e. green circles for Seyfert 1s (labelled Sy 1s) and orange triangles for Seyfert 2s (labelled Sy 2s). The solid curve in the left panel shows a simple power-law fit with $M_{\text{BH}} \propto (L_{\text{X}}/L_{\text{Edd}})^{-1.13 \pm 0.15}$.

not directly demonstrated. In this work, we reanalyze the complete hard-X-ray selected Seyfert galaxy sample of P15, with an emphasis on comparison between different type of sources (radio loud versus radio quiet, Seyfert 1s versus Seyfert 2s, etc). For tens of sources we update their measurements in black hole mass and radio luminosity. This work is organized as follows. In Section 2, we briefly introduce the sample, with a focus on those updates compared to P15. The statistical method is also introduced here. Then in Section 3 we present our results in detail, where we compare properties among different subsamples. Section 4 is devoted to discussions of our results and the final Section 5 provides a brief summary. Throughout this work, the distances are derived based on a flat cold dark matter cosmology (Λ CDM cosmology) with the Hubble constant $H_0 = 70 \text{ km s}^{-1} \text{ Mpc}^{-1}$ and the mass density fraction parameter $\Omega_{\text{M}} = 0.3$.

2 SAMPLE AND STATISTICAL METHOD

2.1 Sample

Our parent sample comes from P15, who compiled a complete sample of moderately bright AGNs, selected at hard X-rays (20-100 keV) from the third *INTEGRAL*/IBIS survey. The sensitivity of *INTEGRAL*/IBIS above 20 keV is better than a few mCrab. Blazars are excluded in this sample, in order to avoid strong Doppler boosting effect (thus the luminosities measured are far away from their intrinsic values). The absorption-corrected 2-10 keV X-ray flux is from Malizia et al. (2009), where they gather from literature. The radio data of the P15 sample mainly come from the NRAO VLA Sky Survey (NVSS; Condon et al. 1998) at 1.4 GHz, whose sensitivity is about $0.45 \text{ mJy beam}^{-1}$. Additional complements are from the Sydney University Molonglo Sky Survey (SUMSS; Bock et al. 1999) at 843 MHz. In total there are 79 Seyfert galaxies in the P15 sample, among which 46 are Seyfert 1s (Seyfert 1-1.5, also include 6 narrow-line AGNs) and 33 are Seyfert 2s (Seyfert 1.9-2.0).

For our investigation, detections/measurements of M_{BH} , L_{R} , and L_{X} are necessary. We complement the M_{BH} of some sources from other literature. For those that lack M_{BH} estimation (noted as “2” in the column 6 of Table 1), we follow Graham (2007) to estimate their M_{BH} as $\log(M_{\text{BH}}/M_{\odot}) = -0.37(\pm 0.04) \times (M_{\text{K}} + 24) + 8.29(\pm 0.08)$. Here the absolute K-band magnitude of the galaxy M_{K}

is obtained from Two-Micron All-Sky Survey (2MASS) through SIMBAD.⁴ This above empirical relationship has a total scatter of 0.33 dex in M_{BH} (Graham 2007), similar to those derived based on other methods. We exclude from our final sample sources that lack detections/measurements of either M_{BH} , L_{R} , or L_{X} . We further examined their radio fluxes at 1.4 GHz, to consider only the radio emission from the nuclei/core region. This is crucial for those resolved ones with extended structures. For those resolved ones, if possible, their nuclear radio emission at 1.4 GHz is then derived from higher-resolution (compared to VLA) VLBI⁵ observations at frequencies specified below, assuming a radio spectrum $F_{\nu} \propto \nu^{-\alpha}$ with $\alpha = 0.7$ (the same as P15), except for 2 sources that have reliable α measurements, i.e. NGC 1275 ($\alpha = -0.51$, Kim et al. 2019) and NGC 5506 ($\alpha = -0.06$, Middelberg et al. 2004). Compared to P15, sources that have their radio fluxes updated are: NGC 1275 (based on VLBI observations at 43 GHz, Kim et al. 2019), NGC 3783 (1.6 GHz, Orienti & Prieto 2010), NGC 4151 (5 GHz, Nagar et al. 2005), NGC 4388 (1.6 GHz, Giroletti & Panessa 2009), NGC 5506 (1.6 GHz, Middelberg et al. 2004), 3C 390.3 (5 GHz, Dodson et al. 2008), Cyg A (1.34 GHz, Struve & Conway 2010) and 4C 74.26 (2.3 GHz, Bourda et al. 2011).

To summarize, of the original 79 AGNs in P15, 9 (4) are excluded due to the lack of radio (BH mass) measurements. The other 2 are also excluded, who are only detected marginally or suffer background contamination in radio. Our final sample includes 64 sources, among which 35 are Seyfert 1s (Seyfert 1-1.5, 4 narrow-line Seyfert 1s are also included) and 29 are Seyfert 2s (Seyfert 1.9-2.0). We list in Table 1 the basic properties of our sample, including their Seyfert classification, redshift, black hole mass and the method adopted in its measurement, X-ray luminosities in 2-10 keV (L_{X}) and 20-100 keV (L_{HX} ; from *INTEGRAL*/IBIS, see P15), and radio luminosities at 1.4 GHz. Their radio morphology and the size of the radio core at 1.4 GHz (NVSS) or 0.8 GHz (SUMSS) are also provided for reference.

Figure 1 shows the basic properties of our sample. In both panels, the optical property is defined by the color and the shape, i.e. the

⁴ <http://simbad.u-strasbg.fr/simbad/>

⁵ very long baseline interferometry, e.g., the *Very Long Baseline Array* (VLBA) and the *European VLBI Network* (EVN).

Table 1. Basic properties of the *INTEGRAL*/*IBIS* hard-X-ray selected Seyfert sample

Name (1)	Class (2)	z (3)	$\text{Log}(M_{\text{BH}})$ (4)	M_{BH} Method (5)	Ref. (6)	$\text{Log}(L_X)$ (7)	$\text{Log}(L_{\text{HX}})$ (8)	$\text{Log}(L_R)$ (9)	Radio Mor.* (10)	D_{maj} (11)
IGR J00333+6122	Sy 1.5	0.105	8.5	GR	1	44.19	44.44	39.46	U	< 49.09
NGC 788	Sy 2	0.0136	7.5	WL	1	42.86	43.29	37.61	R	35.6
NGC 1068	Sy 2	0.0038	7.2	WL	1	42.95	43.35	39.27	R	18.95
QSO B0241+62	Sy 1	0.044	8.1	WL	4	43.87	44.41	40.3	U	< 20.57
NGC 1142	Sy 2	0.0288	9.4	WL	1	43.82	43.96	39.53	U	< 13.46
B3 0309+411	Sy 1	0.136	8.8	M_K	2	45.04	44.99	41.27	R	1373
NGC 1275	Sy 2	0.0175	8.5	WL	1	42.89	43.38	39.60 (a)	R	109.1
3C 111	Sy 1	0.0485	9.6	WL	1	44.52	44.66	41.38	R	393.0
LEDA 168563	Sy 1	0.029	8.0	M_K	1	43.9	44.04	38.48	S	15.68
4U 0517+17	Sy 1.5	0.0179	7.0	RM	1	43.23	43.62	37.75	S	8.484
MCG+08-11-11	Sy 1.5	0.0205	8.1	WL	1	43.69	43.74	39.45	R	84.34
Mrk 3	Sy 2	0.0135	8.7	WL	1	44.17	43.79	39.76	U	< 6.311
Mrk 6	Sy 1.5	0.0188	8.2	WL	1	43.27	43.57	39.43	U	< 8.789
IGR J07565-4139	Sy 2	0.021	8.0	M_K	3	42.14	43.21	37.84	S*	14.05
IGR J07597-3842	Sy 1.2	0.04	8.3	GR	1	43.9	44.11	38.24	U	< 18.7
ESO 209-12	Sy 1	0.0396	9.0	M_K	2	43.43	43.87	29.23	S*	36.7
FRL 1146	Sy 1.5	0.0316	8.7	M_K	2	43.39	43.56	38.61	R	94.55
SWIFT J0917.2-6221	Sy 1	0.0573	9.9	G	1	44.17	44.17	39.6	S*	35.35
MCG-05-23-16	Sy 2	0.0085	6.3	WL	1	43.09	43.34	37.47	U	< 3.974
IGR J09523-6231	Sy 1.9	0.252	7.6	WL	1	45.28	45.22	40.02	U*	< 112.6
SWIFT J1009.3-4250	Sy 2	0.033	8.8	M_K	2	42.96	43.81	38.74	S*	28.52
NGC 3281	Sy 2	0.0115	8.0	WL	1	43.68	43.35	38.45	U	< 5.376
IGR J10404-4625	Sy 2	0.2392	8.5	S	4	44.93	45.58	40.84	S*	204
NGC 3783	Sy 1	0.0097	7.5	WL	1	43.07	43.42	37.24 (b)	R	55.63
IGR J12026-5349	Sy 2	0.028	8.0	S	4	43.11	43.81	39.06	R	143.1
NGC 4151	Sy 1.5	0.0033	7.5	WL	1	43.05	43.16	37.07 (c)	U	< 1.543
NGC 4388	Sy 2	0.0084	7.2	WL	1	43.0	43.54	36.58 (d)	R	49.22
NGC 4507	Sy 2	0.0118	7.6	WL	1	43.08	43.7	38.28	S	8.086
LEDA 170194	Sy 2	0.036	8.9	WL	1	43.48	44.22	39.13	R	130.2
NGC 4593	Sy 1	0.009	7.0	WL	1	42.8	43.09	37.18	R	35.9
IGR J12415-5750	Sy 1	0.023	8.0	GR	1	42.93	43.4	38.37	S*	15.83
NGC 4945	Sy 2	0.0019	6.2	WL	1	42.2	42.55	38.62	R	27.0
Cen A	Sy 2	0.0018	8.0	WL	1	42.36	42.7	39.35	R*	33.66
NGC 5252	Sy 2	0.023	9.0	WL	1	43.72	43.71	38.39	U	< 10.75
IC 4329A	Sy 1.2	0.016	7.0	WL	1	43.74	44.06	38.67	R	113.7
Circinus Galaxy	Sy 2	0.0014	6.0	WL	1	42.39	42.15	37.64	R*	16.41
NGC 5506	Sy 1.9	0.0062	6.7	WL	1	42.83	42.85	37.82 (e)	U	< 2.898
ESO 511-G030	Sy 1	0.2239	8.7	M_K	1	45.13	45.56	40.08	R	224.8
IGR J14515-5542	Sy 2	0.018	7.6	WL	4	42.68	43.04	38.19	S*	11.79
IC 4518A	Sy 2	0.0163	7.5	G	1	42.83	43.09	39.05	R*	71.12
IGR J16024-6107	Sy 2	0.011	7.4	M_K	2	41.66	42.46	37.49	U*	< 4.914
IGR J16351-5806	Sy 2	0.0091	8.6	M_K	2	42.51	42.74	38.22	R*	30.63
IGR J16385-2057	NLS1	0.0269	6.8	GR	1	43.02	43.39	38.13	S	15.34
IGR J16482-3036	Sy 1	0.031	8.2	GR	1	43.6	43.79	37.89	R	112.1
IGR J16558-5203	Sy 1.2	0.054	7.9	GR	1	44.33	44.31	38.65	U*	< 24.12
NGC 6300	Sy 2	0.0037	5.5	WL	1	41.87	42.28	36.92	R*	20.3
GRS 1734-292	Sy 1	0.0214	8.9	WL	1	43.56	43.9	38.79	U	10.0
2E 1739.1-1210	Sy 1	0.037	8.2	GR	1	43.56	43.89	38.13	U	17.3
IGR J18027-1455	Sy 1	0.035	7.6	WL	4	43.23	44.04	38.51	R	144
ESO 103-35	Sy 2	0.0133	7.1	WL	1	43.26	43.49	38.1	U*	< 5.941
3C 390.3	Sy 1	0.0561	8.5	WL	1	44.34	44.6	40.49 (f)	R	419.6
2E 1853.7+1534	Sy 1	0.084	8.2	GR	1	44.25	44.56	38.86	U	< 39.27
IGR J19378-0617	NLS1	0.0106	6.8	WL	1	42.91	42.64	38.11	U	< 4.955
NGC 6814	Sy 1.5	0.0052	7.1	WL	1	40.98	42.52	37.07	R	27.88
Cyg A	Sy 2	0.0561	9.4	G	1	44.68	44.73	40.69 (g)	R	468.6
4C 74.26	Sy 1	0.104	9.6	WL	1	44.75	45.04	40.52 (h)	R	1724.0
S52116+81	Sy 1	0.084	8.8	WL	1	44.25	44.77	40.71	R	701.6
IGR J21247+5058	Sy 1	0.02	6.6	WL	1	43.81	43.96	39.51	R	279.3
SWIFT J2127.4+5654	NLS1	0.014	7.2	GR	1	42.89	43.04	37.53	S	7.918
RX J2135.9+4728	Sy 1	0.025	7.5	WL	4	43.00	43.32	38.08	U	< 11.69
NGC 7172	Sy 2	0.0087	7.7	WL	1	42.51	43.11	37.87	R	36.88
MR 2251-178	Sy 1	0.064	6.9	WL	1	44.23	44.79	39.26	U	< 29.92
MCG-02-58-22	Sy 1.5	0.0469	7.1	WL	1	44.16	44.25	39.29	U	< 21.93
IGR J23308+7120	Sy 2	0.037	8.4	M_K	2	42.80	43.55	37.92	S	40.31

Notes: Column 1 – source name; Column 2 – Seyfert classification; Column 3 – redshift; Column 4 – BH mass, Column 5 and 6 – measurement method and reference for BH mass; Columns 7 and 8 – X-ray luminosities in 2-10 keV (L_X) and 20-100 keV (L_{HX}); Column 9 – radio luminosities at 1.4 GHz; Column 10 – radio morphology; Column 11 – length of half the major axis of the radio core. M_{BH} in unit M_{\odot} , luminosities in unit erg s^{-1} , and D_{maj} in unit kpc.

BH mass measurement method (Column 5). RM: reverberation mapping; S: from stellar velocity dispersion; GR: from gas velocity and size of the broad-line region; WL: from the line width and luminosity of broad emission lines (e.g., $\text{H}\beta$, $\text{H}\alpha$, $\text{Pa}\beta$), sometimes the luminosity may be that at 5100Å; G: from gas velocity dispersions (through e.g., $[\text{O III}]$ or $[\text{Ne III}]$); M_K : from K-band magnitude/luminosity of either the whole host galaxy or the stellar bulge;

References for BH mass (Column 6). 1 – P15; 2 – this work; 3 – Khorunzhev et al. (2012); 4 – The Swift/BAT AGN Spectroscopic Survey: <http://www.bass-survey.com/>.

References for L_R (Column 7). (a) Kim et al. (2019); (b) Orienti & Prieto (2010); (c) Nagar et al. (2005); (d) Giroletti & Panessa (2009); (e) Middelberg et al. (2004); (f) Dodson et al. (2008); (g) Struve & Conway (2010); (h) Bourda et al. (2011). The rest L_R measurements are directly from P15.

* *The symbol of the radio morphology (see P15 for details).* U for unresolved, S for slightly resolved, R for resolved and A for ambiguous. Here, sources labelled with * are from the SUMSS survey, while the rest are from the NVSS survey.

Seyfert 1s are shown by green circles and the Seyfert 2s by orange triangles. All sources in our sample is fairly bright. The X-ray Eddington ratio L_X/L_{Edd} covers almost 4 orders of magnitude, i.e. between $\sim 10^{-4.2}$ and $\sim 10^{-0.3}$. For an X-ray bolometric correction $L_{\text{bol}}/L_X \approx 16$ (e.g., Ho 2008; Netzer 2019), the Eddington ratio ($\lambda_{\text{Edd}} = L_{\text{bol}}/L_{\text{Edd}}$) of our sample then ranges between $\sim 10^{-3}$ and ~ 10 . The left panel of Figure 1 shows the BH mass distribution, where we find that M_{BH} ranges between $10^{-5.5}M_{\odot}$ and $10^{-10}M_{\odot}$, with a clustering around $10^{7-9}M_{\odot}$. Moreover, there apparently exists a negative correlation between M_{BH} and L_X/L_{Edd} , where a simple power-law fit suggests that $M_{\text{BH}} \propto (L_X/L_{\text{Edd}})^{-1.33 \pm 0.18}$. Pearson correlation coefficient of this fitting is listed in Table 2. The lack of small M_{BH} AGNs at the low- L_X/L_{Edd} end is because our sample is limited by the X-ray flux; the lack of large M_{BH} AGNs at the high- L_X/L_{Edd} end, on the other hand, is because of the cosmic evolution, i.e. galaxies in local universe, whose M_{BH} is expected to be larger, are less active than those distant ones.

We also separate radio-loud sources (open symbols in Figure 1) from radio-quiet ones (filled symbols), where the X-ray radio-loudness R_X is defined as $R_X = L_R/L_X$ (Terashima & Wilson 2003)⁶ and the RL/RQ boundary is set to $R_X = 10^{-4.5}$. We emphasize that we do not observe, in our near-complete hard X-ray selected AGN sample, the bimodal distribution of R_X (see also Figure 2 of P15), suggesting that the bimodality in radio-loudness may be a selection effect. Another property of our sample is that, as L_X/L_{Edd} increases, the fraction of RL sources declines significantly, i.e. there are only two RL AGNs in the $L_X/L_{\text{Edd}} > 10^{-2}$ regime. One is IGR J10404-4625 whose $L_X/L_{\text{Edd}} \approx 0.02$, and the other is IGR J21247+5058 whose $L_X/L_{\text{Edd}} \approx 0.13$.

2.2 Statistical Method and Basic Assumptions

As clearly shown in the left panel of Figure 1, there is a strong $M_{\text{BH}} - L_X/L_{\text{Edd}}$ relationship, which obviously contaminates the estimation of ξ_M in Equation 1. To avoid this technical problem, we in this work aggressively omit the dependence on ξ_M but focus on ξ_X , i.e. we consider the following radio/X-ray correlation in Eddington unit,

$$\log(L_R/L_{\text{Edd}}) = \xi_X \log(L_X/L_{\text{Edd}}) + \text{const.} \quad (3)$$

Since most sources have a clustering of M_{BH} at $\sim 10^{7-9}M_{\odot}$, physically it is equivalent to the case of absorbing the impact of M_{BH} into const. .

Following Merloni et al. (2003), we statistically fit the observational data through the minimization of the following quantity (hereafter the least χ^2 approach),

$$\chi^2 = \sum \frac{(\log(L_R/L_{\text{Edd}}) - \xi_X \log(L_X/L_{\text{Edd}}) - \text{const.})^2}{(\sigma_{R,\text{Edd}} \log(L_R/L_{\text{Edd}}))^2 + (\xi_X \sigma_{X,\text{Edd}} \log(L_X/L_{\text{Edd}}))^2}. \quad (4)$$

Considering the non-simultaneity of the radio and X-ray fluxes used in this work, we ignore the observational uncertainties in $\log(L_R/L_{\text{Edd}})$ and $\log(L_X/L_{\text{Edd}})$, but directly take their uncertainties to be $\sigma_{R,\text{Edd}} = 0.3$ and $\sigma_{X,\text{Edd}} = 0.3$, respectively (see e.g., Merloni et al. 2003; Gültekin et al. 2009; Xie & Yuan 2017).

We note that in Equation 4 we additionally weight the uncertainties by luminosities in Eddington unit (i.e., L_R/L_{Edd} , L_X/L_{Edd}). This is equivalent to an emphasis on fainter sources. We test this revised regression method through data sets which are manually

⁶ Note that conventionally the radio loudness R is defined as the ratio of luminosities between 5 GHz radio band and the optical B-band (e.g., Kellermann et al. 1989).

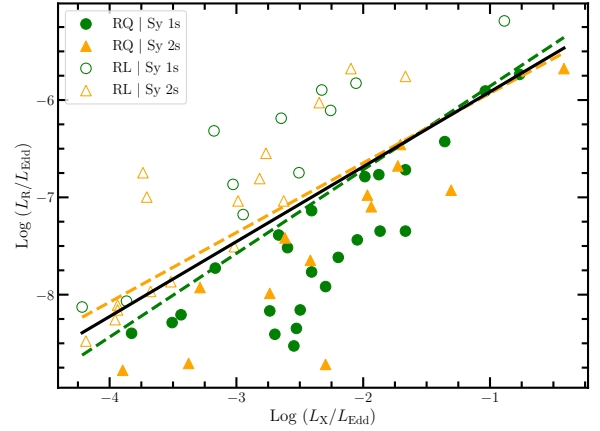


Figure 2. Radio/X-ray correlation (in Eddington units) for Seyfert galaxies, with a comparison between Seyfert 1s (the green filled circles) and Seyfert 2s (the orange filled triangles). The black solid curve represents the fitting to the whole sample (see Equation 5), while the dashed curves provide the fitting results of two subsamples (see Equation 6), with the color the same to those of the data points.

generated by given parameters of ξ_X , $\sigma_{R,\text{Edd}}$ and $\sigma_{X,\text{Edd}}$. We find that the regression based on Equation 4 provides a better recovery of the input ξ_X value than that by original formulae of Merloni et al. (2003).

3 RESULTS

3.1 X-ray flux ratio L_{HX}/L_X distribution

We first investigate the distribution of X-ray flux ratio L_{HX}/L_X as a function of L_X/L_{Edd} . We caution that L_{HX} and L_X are not observed in a coordinated manner, the time interval can be as large as several years (Malizia et al. 2009; P15). AGNs are known to be variable on year timescale (Ulrich, Maraschi & Urry 1997; Netzer 2008), thus L_{HX}/L_X may suffer this non-simultaneity issue.

As shown in the right panel of Figure 1, we find that most sources have $L_{\text{HX}}/L_X \sim 1 - 4$, despite the non-simultaneity issue. Moreover, statistically there is no dependence of the ratio L_{HX}/L_X on the X-ray luminosity L_X/L_{Edd} . Furthermore, we separate the sources according to their radio-loudness and Seyfert classification. Still, we do not observe any separation in L_{HX}/L_X between RL and RQ ones, nor between Seyfert 1s and Seyfert 2s. All these results may imply that, despite the four-order-of-magnitude dynamical range in L_X/L_{Edd} , the possible change in accretion mode (i.e. cold accretion at $L_X/L_{\text{Edd}} \gtrsim 10^{-3}$ versus hot accretion at $L_X/L_{\text{Edd}} \lesssim 10^{-3}$), and the huge difference in their radio loudness and/or Seyfert classification, all the sources in our sample have the same radiative mechanism and origin in X-rays.⁷ From a theoretical point of view, the most plausible mechanism is hot accretion flow (or corona in case of cold accretion).

⁷ We note that, the jet may also dominate the X-rays in RL AGNs (Harris & Krawczynski 2006; Blandford, Meier, & Readhead 2019); and radio origin may also be diverse (Panessa et al. 2019; Chiaraluce et al. 2020). See also Introduction.

3.2 Radio/X-ray Correlation in Seyfert Galaxies

The key motivation of this work is to investigate ξ_X , i.e. the radio/X-ray correlation slope, among different types of Seyfert AGNs. We take three different classification methods, i.e. according to, 1) the full width at half-maximum (FWHM) of the emission lines in optical band, 2) the radio loudness R_X , and 3) the size of radio-emission site.

3.2.1 impact of optical emission-line properties

We first consider their differences in optical emission-line properties, i.e. Seyfert 1s versus Seyfert 2s. There are 35 (~52%) Seyfert 1s and 29 (~48%) Seyfert 2s. We plot in the Figure 2 all the sources in the revised ($\log(L_R/L_{\text{Edd}}), \log(L_X/L_{\text{Edd}})$) plane, where Seyfert 1s are shown by green filled circles and Seyfert 2s are shown by orange filled triangles.

Several results can be derived immediately. First, the observations do exhibit large scatters (see also Merloni et al. 2003; Falcke et al. 2004), i.e. at a given X-ray luminosity L_X/L_{Edd} , the nuclear radio luminosity L_R/L_{Edd} can differ by 2-3 orders of magnitude, and the scatter is similar among Seyfert 1s and Seyfert 2s. This may suggest as a piece of evidence against the AGN unification model, where viewing angle is considered as the primary factor, i.e. face-on for Seyfert 1s and edge-on for Seyfert 2s (see, e.g., Netzer 2015; Padovani et al. 2017 for a summary of additional evidence against the unification model).⁸ Actually, we notice from this plot that Seyfert 1s and Seyfert 2s overlap each other in L_R/L_{Edd} , suggesting that beaming effect is not the key factor. Based on our current understanding of jet physics, we may argue that additional factor(s), among which likely the magnetic flux (Sikora et al. 2007) and/or the BH spin (Ünal & Loeb 2020), should play dominate roles in introducing the scatters as observed.

Another result from this plot is that, the Seyfert 1s and Seyfert 2s cover a similar range in both radio and X-ray luminosities (in Eddington unit), although as shown in Figure 1 the Seyfert 2s are less massive in M_{BH} compared to Seyfert 1s, especially at the bright L_X/L_{Edd} regime.

We fit the data under the least χ^2 approach. As shown by the black solid curve in Figure 2, the whole sample follows

$$\log(L_R/L_{\text{Edd}}) = 0.77^{+0.10}_{-0.10} \log(L_X/L_{\text{Edd}}) - 5.15^{+0.25}_{-0.25}. \quad (5)$$

Meanwhile, the Seyfert 1s and Seyfert 2s follow, respectively,

$$\log(L_R/L_{\text{Edd}}) = 0.86^{+0.15}_{-0.15} \log(L_X/L_{\text{Edd}}) - 5.00^{+0.36}_{-0.36}, \quad (\text{Sy 1s})$$

$$\log(L_R/L_{\text{Edd}}) = 0.72^{+0.13}_{-0.13} \log(L_X/L_{\text{Edd}}) - 5.22^{+0.35}_{-0.35}. \quad (\text{Sy 2s})$$

(6)

The coefficients of Pearson correlation analysis are listed in Table 2. The slopes in the two subsamples agree with each other within $\sim 1\sigma$. This implies that, either orientation is not the key difference between Seyfert 1s and Seyfert 2s (thus disfavour the AGN unification model), or there is no intrinsic difference in the origin of X-ray emission.

3.2.2 impact of radio-loudness

We then explore the impact of radio-loudness, which is widely considered as an indicator of jet beaming effect. According to our

⁸ Indeed some individual AGNs, so-called changing-look AGNs, can change their appearances in optical emission lines (i.e. between type 1 with broad lines and type 2 with only narrow lines) over several years (e.g., LaMassa et al. 2015), a period that the orientation should not vary much.

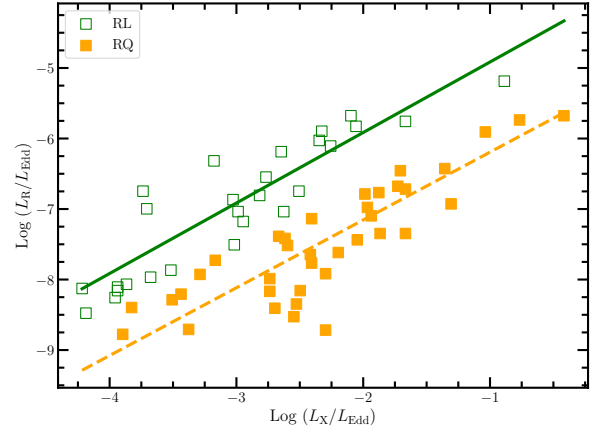


Figure 3. Radio/X-ray correlation (in Eddington units) for Seyfert galaxies with different radio loudness R_X . Here the green open squares are for RL AGNs and the orange filled squares for RQ ones. The fitting results are also shown (see Equation 7), with the color the same to that of the data points.

RL/RQ separation ($R_X = 10^{-4.5}$; Terashima & Wilson 2003), 27 out of 64 (~42%) sources are RL and the rest 37 out of 64 (~58%) sources are RQ. Such a high fraction of RL sources (compared to the typical 10% in bright AGNs and quasars) is known in literature (e.g., Ho 2008). Because of the classification, RL AGNs are systematically brighter in radio luminosity L_R/L_{Edd} , at a given X-ray luminosity L_X/L_{Edd} .

We re-plot the sample in Figure 3, where RL AGNs are shown by green open squares and RQ AGNs are shown by orange filled squares. We find that most RL AGNs in our sample are less luminous in X-rays, only two out of 27 RL AGNs (~7%), i.e. IGR J10404-4625 and IGR J21247+5058, is bright with $L_X/L_{\text{Edd}} > 10^{-2}$. On the other hand, for the 14 bright RQ AGNs with $L_X/L_{\text{Edd}} > 10^{-2}$, there is no preference in Seyfert types (see the left panel of Figure 1), i.e. 8 sources are Seyfert 1s and the rest 6 sources are Seyfert 2s.

We fit the data with least χ^2 regression method and find that RL and RQ AGNs follow, respectively,

$$\log(L_R/L_{\text{Edd}}) = 1.00^{+0.09}_{-0.09} \log(L_X/L_{\text{Edd}}) - 3.92^{+0.25}_{-0.25}, \quad (\text{RL AGNs})$$

$$\log(L_R/L_{\text{Edd}}) = 0.96^{+0.08}_{-0.08} \log(L_X/L_{\text{Edd}}) - 5.23^{+0.18}_{-0.18}. \quad (\text{RQ AGNs})$$

(7)

The coefficients of Pearson correlation analysis are listed in Table 2. Again, the correlation slopes of RL and RQ AGNs are consistent with each other at 1σ uncertainty level,

Our result of a $\xi_X \sim 1$ FP in RL AGNs agrees with that reported in Liao et al. (2020). They investigated a sample of young radio AGNs, which all have radiatively efficient accretion (e.g., cold accretion) and powerful radio emission. Most previous work find that RL AGNs follow a much steeper relationship, i.e. $\xi_X \sim 1.3$ (e.g., Panessa et al. 2007; Li, Wu & Wang 2008; de Gasperin et al. 2011), and the correlation becomes steeper (i.e., larger ξ_X) as the radio-loudness increases (Li, Wu & Wang 2008). In accretion theory, the standard FP is achieved when the hot accretion flow is responsible for the X-rays (Yuan & Cui 2005; Xie & Yuan 2016); the steep $\xi_X \sim 1.3$ FP can be observed when the X-rays originates from the relativistic jet rather than the hot accretion flow (see e.g., discussions in Yuan & Cui 2005; Xie & Yuan 2017). Such a situation can only be achieved under two conditions, one is when the system is faint enough (e.g., $L_X/L_{\text{Edd}} \leq 10^{-6}$; Yuan, Cui & Narayan 2005; Xie & Yuan 2017), and the other is when the beaming effect is sufficiently strong (high

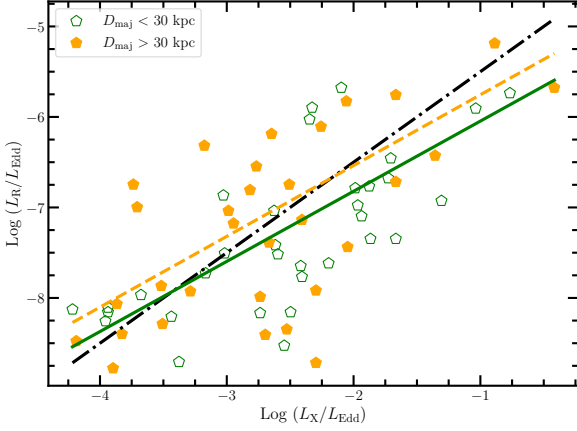


Figure 4. Radio/X-ray correlation (in Eddington units) for Seyfert galaxies with different radio emission size. The green open pentagons and orange filled pentagons are respectively, for sources with their radio size (length of the half major axis) are less or greater than 30 kpc. The fitting results are also shown, with the color the same to those of the data points.

Doppler boosting effect for the jet emission in X-rays; e.g., Panessa et al. 2007; Li, Wu & Wang 2008). In this theoretical picture, our finding of a universal ξ_X among RL and RQ systems suggests that the X-rays of RL Seyferts also originate from hot accretion flow, the same as RQ Seyferts. This interpretation is also favoured by the L_{HX}/L_X distribution, as shown in Figure 1. We note that similar results have been reported in literature. For example, based on a compilation of 13 low-excitation radio galaxies (LERGs; belong to RL AGNs in our classification), Li & Gu (2018) find the LERGs to follow the standard ξ_X correlation, not a steep one as reported in de Gasperin et al. (2011). The difference is that in the latter work they also include LERGs which have a steep radio spectrum.

Finally, we caution that the RQ systems here also agree with the linear $L_R/L_X \sim 10^{-5}$ relationship observed in corona-active stars, thus being explained under an AGN corona (above the SSD) model (Laor & Behar 2008; see Sec 4.1).

3.2.3 impact of emission size in radio

We finally investigate the impact of the radio emission size. It is naturally expected that, the velocity and power of jet, which can be illustrated by the radio morphology, are crucial to determining the interaction between the jet and the host galaxy (e.g., McNamara & Nulsen 2012; Duan & Guo 2020). Again we caution that the jet interpretation of RQ AGNs may be an over-simplification, see Sec. 4.1. More than 50% sources in our sample do not show clear extended structure.⁹ The only source with FR I jet morphology is NGC 1275, and the 5 sources with FR II jet morphology are respectively, B3 0309+411, 3C 111, 3C 390.3, Cyg A and 4C 74.26. We thus take the length of half the major axis D_{maj} as a representative of the radio morphology. We take observations of either NVSS (at 1.4 GHz) or SUMSS (at 0.8 GHz) (see Sec. 2.1 and Table 1), and define jets whose $D_{\text{maj}} < 30$ kpc as compact systems, and those whose $D_{\text{maj}} > 30$ kpc as extended (or resolved) systems. Under

⁹ It is well-known that jet in RL AGNs morphologically has a Fanaroff–Riley dichotomy distribution, with the core-dominant FR I jets being shorter and less stable than the lobe-dominant FR II jets (Fanaroff & Riley 1974).

Table 2. Pearson correlation analysis of each subsample

Sample (No.)	Pearson	P_{null}	R^2
Figure 1: $\log(M_{\text{BH}})$ vs. $\log(L_X/L_{\text{Edd}})$			
full sample (64)	-0.54	3.2×10^{-6}	0.54
Figure 2–4: $\log(L_R/L_{\text{Edd}})$ vs. $\log(L_X/L_{\text{Edd}})$			
full sample (64)	0.66	2.9×10^{-9}	0.49
Sy 1s (35)	0.65	2.6×10^{-5}	0.56
Sy 2s (29)	0.67	3.9×10^{-5}	0.45
RQ (37)	0.86	9.2×10^{-12}	0.76
RL (27)	0.91	7.0×10^{-11}	0.81
Compact (33)	0.71	3.3×10^{-6}	0.56
Extended (31)	0.64	1.2×10^{-4}	0.45
Figure 5: $\log(\eta_{\text{jet}})$ vs. $\log(L_X/L_{\text{Edd}})$			
full sample (64)	-0.44	2.9×10^{-4}	0.36

Notes: Column 1 – sample; Column 2 and 3 – Pearson correlation coefficient and null correlation hypothesis probability; Column 4 – goodness of fit, defined as ESS (Explained Sum of Squares) divided by TSS (Total Sum of Squares). The closer the R^2 is to 1, the better the fitting is. Check http://online.sfsu.edu/mbar/ECON312_files/R-squared.html for detail definition of the R^2 .

this definition, 31 Seyferts in our sample belong to the extended category, and the rest 33 Seyferts belongs to the compact category.

We show the results in Figure 4, where the green open pentagons and orange filled pentagons are respectively, for sources with their D_{maj} are less or greater than 30 kpc. Obviously there is no clear separation in the $L_R/L_{\text{Edd}} - L_X/L_{\text{Edd}}$ plane between systems with these two types of radio morphologies, i.e. they overlap with each other. Moreover, with a comparison to Figure 3, we find that there is no direct connection between radio emission size and the radio-loudness, i.e. 11 out of 27 (41%) RL AGNs remain compact with $D_{\text{maj}} < 30$ kpc; and 15 out of 37 (41%) RQ AGNs show extended radio emission. When $L_X/L_{\text{Edd}} \gtrsim 10^{-2}$, there is a weak tendency that Seyferts with extended radio morphology are more luminous in L_R/L_{Edd} (equivalently, radio-louder) at a given L_X/L_{Edd} . But the sample size in this region is small, and such tendency disappears when $L_X/L_{\text{Edd}} \lesssim 10^{-2}$. We further fit the data with least χ^2 regression method and find that Seyferts with compact and extended radio emission follow respectively (see Table 2 for Pearson correlation coefficients),

$$\begin{aligned} \log(L_R/L_{\text{Edd}}) &= 0.78_{-0.13}^{+0.13} \log(L_X/L_{\text{Edd}}) - 5.27_{-0.32}^{+0.32}, & (\text{Compact}) \\ \log(L_R/L_{\text{Edd}}) &= 0.78_{-0.14}^{+0.14} \log(L_X/L_{\text{Edd}}) - 4.97_{-0.37}^{+0.37}. & (\text{Extended}) \end{aligned} \quad (8)$$

Clearly, the correlation slopes are consistent with each other within 1σ uncertainty level.

Finally, we note that we also check different choices of D_{maj} criteria, i.e. 20 kpc or 25 kpc, and the results (not shown here) are quite similar to that reported above.

4 DISCUSSIONS

4.1 Alternative Models for the Radio and X-ray emissions in RQ AGNs

One notable limitation of this work is that, we attribute in this work (a dominant fraction of) the nuclear radio emission to be from the jet component, either well-collimated or weakly-collimated. Due to

the low resolution of NVSS and large D_{maj} in our sample, alternative contributions indeed cannot be ruled out, especially in RQ systems.

Unlike RL systems, many RQ Seyferts do not show jet-like structure in high-resolution radio observations (e.g., [Ulvestad, Antonucci & Barvainis 2005](#) and references therein): some remain unresolved at sub-pc scale, while others are extended but lack linear (jet-like) morphology. We notice that the origin of nuclear radio and/or X-ray emission in RQ Seyferts is actually under active debate in recent years (e.g., [Bonchi et al. 2013](#); [Baek et al. 2019](#); [Laor et al. 2019](#); [Smith et al. 2020](#); [Fischer et al. 2021](#), and references therein.); alternative origins of radio emission in RQ AGNs include star formation, AGN wind and AGN corona (see e.g., [Padovani et al. 2017](#); [Panessa et al. 2019](#) for reviews). Below we provide brief discussions on these alternative origins.

One origin is the nuclear star formation activities. Active star formation processes will provide extended emission in radio and near-infrared. Based on a VLA 22 GHz RQ AGN sample, [Smith et al. \(2020\)](#) report that, after core flux subtraction, AGN with compact morphology will drop below the star formation expectation. This implies that the radio emission from nuclear star formation is still unresolved even at 1 arcsecond resolution. Higher resolution (or at higher frequency) observations are thus necessary. However, AGN activities co-evolve with the dynamics of the circum-nuclear medium, where a tight connection to nuclear star formation is a direct signature (e.g., [Zhuang et al. 2021](#)). In this understanding, the star formation scenario for the non-linear radio emission awaits additional evidence. We also emphasize that the dominant mechanism for radio emission at different frequencies might be different (e.g., in star-forming galaxies, free-free emission will become comparable important to synchrotron at high frequency).

Another scenario proposed in literature is a hot corona (above the cold SSD) model for not only X-rays but also radio ([Laor & Behar 2008](#)) in the RQ systems. This model is similar to the corona in stellar systems, where a linear $L_{\text{R}}/L_{\text{X}} \sim 10^{-5}$ relationship is established ([Guedel & Benz 1993](#)). Observationally the RQ sources seem to be broadly consistent with this model (e.g., [Smith et al. 2020](#) and references therein). We note that our interpretation shares the same origin of X-rays, but differs in the origin of radio emission, i.e. in their model from non-thermal or hot thermal electrons in the corona ([Laor & Behar 2008](#); [Raginski & Laor 2016](#)), or in our interpretation from non-thermal electrons in the weakly-collimated jet. One supporting evidence of wind or corona scenario is from [Li, Wu & Wang \(2008\)](#), where they found that the broad line luminosity is tight correlated with radio luminosity in RQs, i.e. the radio emission in RQs might be nearly isotropic.

Our result suggests a universal radio/X-ray correlation in Seyferts, irrelevant to radio-loudness. However, the uncertainties in ξ_{X} are still large, thus although we favor the jet interpretation, we actually cannot rule out any alternative scenarios, especially because all these processes correlate with each other. In principle, the contribution of nuclear star formation process can be removed from regular monitoring of individual sources, since the AGN and stellar processes have different variability timescale; the corona and wind/outflow models, on the other hand, are tightly correlated to the accretion process, thus challenge to discriminate.

4.2 Jet Production Efficiency η_{jet}

One important quantity in accretion theory is the jet production efficiency η_{jet} , which characterizes the fraction of accretion power that enters into the relativistic jet (e.g., [van Velzen & Falcke 2013](#); [Ghisellini et al. 2014](#); [Inoue et al. 2017](#); [Rusinek et al. 2020](#); [Soares](#)

[& Nemmen 2020](#); [Wójtowicz et al. 2020](#)). It is defined as,

$$\eta_{\text{jet}} = \frac{P_{\text{jet}}}{\dot{M}c^2}. \quad (9)$$

Obviously, the jet production efficiency η_{jet} will also dependent on magnetic flux attached to jet and the BH spin. Based on a sample of ~ 7000 radio-loud quasars, [Inoue et al. \(2017\)](#) reported an efficiency of $\eta_{\text{jet}} \approx 1 \times 10^{-2}$ in the cold accretion disc regime, suggesting the BH spin and/or the magnetic flux are low in these systems; while based on a sample of ~ 200 well-selected blazars with γ -ray detection, [Ghisellini et al. \(2014\)](#) find that their $\eta_{\text{jet}} \sim 1 - 10$.

Here we investigate the jet production efficiency of Seyfert galaxies. There are several methods to estimate the jet power (see [Soares & Nemmen 2020](#) for a brief summary), i.e. the radio lobe emission based on equipartition assumption ([Willott et al. 1999](#)), the radio core-shift effect ([Shabala, Santoso, & Godfrey 2012](#)) and the spectrum modelling ([Ghisellini et al. 2014](#)). In this work we follow that of [Willott et al. \(1999\)](#) (for later updates, see e.g., [Cavagnolo et al. 2010](#)). Based on a sample of 77 RL AGNs that includes both FR Is and IIs, they found that the jet power has a strong correlation with the radio luminosity at 151 MHz, which can be re-expressed as $P_{\text{jet}} \approx 1.9 \times 10^7 f^{3/2} L_{\text{R}}^{6/7} \text{ erg s}^{-1} \approx 6.0 \times 10^8 L_{\text{R}}^{6/7} \text{ erg s}^{-1}$ at 1.4 GHz, if a radio spectrum $F_{\nu} \propto \nu^{-0.7}$ is adopted. The theoretical uncertainties in P_{jet} are absorbed in a parameter f , which we take $f = 10$, following the recent calibrations by studies of X-ray cavity and hot spot in AGNs ([Godfrey & Shabala 2013](#)). We caution that the calibration implies that the derived jet power is a time-averaged (over the past millions of years) one, and may differ from the P_{jet} of the current on-going accretion process (represented by L_{X}). We for simplicity omit this uncertainty. We further caution that the above jet power estimation is from RL AGNs; the application to RQ AGNs may be aggressive and risky, with uncertainties hard to measure. However, this is the only method we currently have.

The accretion power $\dot{M}c^2$ can be estimated from the bolometric luminosity of hot accretion flow $L_{\text{bol,h}}$ ¹⁰ as $\dot{M}c^2 = L_{\text{bol,h}}/\epsilon$, where ϵ is the radiative efficiency. For a geometrically-thin cold accretion disc like SSD ([Shakura & Sunyaev 1973](#)), the efficiency is $\epsilon_{\text{SSD}} \approx 10\%$; while for a hot accretion flow, the efficiency is systematically lower than ϵ_{SSD} , but its value increases as \dot{M} increases ([Xie & Yuan 2012](#); [Xie & Zdziarski 2019](#)), and can be comparable to that of cold SSD at high $\dot{M}/\dot{M}_{\text{Edd}}$ end. We further estimate the $L_{\text{bol,h}}$ from the X-ray bolometric correction factor $f_{\text{X}} = L_{\text{bol,h}}/L_{\text{X}}$ (e.g., [Ho 2008](#); [Vasudevan & Fabian 2009](#)). Then we can re-express Equation (9) as,

$$\frac{\eta_{\text{jet}} f_{\text{X}}}{\epsilon} = \frac{P_{\text{jet}}}{L_{\text{X}}} \propto \frac{L_{\text{R}}^{6/7}}{L_{\text{X}}}. \quad (10)$$

We plot in Figure 5 the relationship between $L_{\text{X}}/L_{\text{Edd}}$ and the jet production efficiency η_{jet} , where the symbols are of the same meaning to those in Figure 1. Here we statistically assume $f_{\text{X}} \approx 16$ ([Ho 2009](#)) and $\epsilon \approx 8\%$ ([Xie & Yuan 2012](#)). The original value of $\eta_{\text{jet}} f_{\text{X}}/\epsilon$ ($\equiv P_{\text{jet}}/L_{\text{X}}$, see Equation 10) of each source is also shown in Figure 5 by its right y-axis. Several results can be derived directly from this plot. First, η_{jet} (or more accurately, $\eta_{\text{jet}} f_{\text{X}}/\epsilon$) shows a pretty large scatter at given X-ray luminosity ($L_{\text{X}}/L_{\text{Edd}}$), and the scatter is similar among RL AGNs and RQ AGNs. On the other hand, there is a tendency that Seyfert 1s has a smaller scatter than Seyfert 2s. For the whole sample of 64 Seyferts, we find that η_{jet} varies between $10^{-5.2}$ and 10^{-2} , with a mean value of $\langle \eta_{\text{jet}} \rangle = 1.9_{-1.5}^{+0.9} \times 10^{-4}$. We note

¹⁰ Expressed as the bolometric disc luminosity, i.e. L_{disc} , in the notation of [Inoue et al. \(2017\)](#).

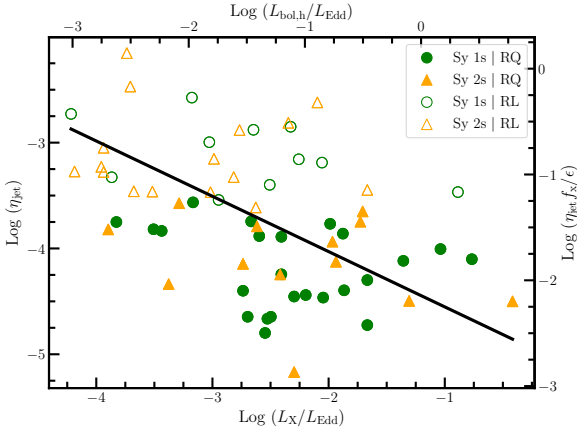


Figure 5. Jet production efficiency η_{jet} as a function of the X-ray Eddington ratio L_X/L_{Edd} (and in the upper x-axis the bolometric Eddington ratio $L_{\text{bol,h}}/L_{\text{Edd}}$), where we assume the radiative efficiency of hot accretion flow $\epsilon = 8\%$ and the X-ray bolometric correction factor $f_X = 16$. The right y-axis shows $\eta_{\text{jet}} f_X / \epsilon \equiv P_{\text{jet}}/L_X$. The black solid curve represents the fitting result to the whole sample, see Equation (12). As labelled in the plot, the symbols are of the same meaning to those in Figure 1.

that compared to the results in literature (van Velzen & Falcke 2013; Ghisellini et al. 2014; Inoue et al. 2017; Soares & Nemmen 2020; Wójtowicz et al. 2020), the scatter is roughly consistent, but the mean value derived here is at least two orders of magnitude smaller. The mean jet production efficiency for RL and RQ subsamples are respectively, $\langle \eta_{\text{jet}} \rangle = 7.9^{+1.9}_{-4.5} \times 10^{-4}$ and $\langle \eta_{\text{jet}} \rangle = 6.9^{+1.7}_{-4.1} \times 10^{-5}$. We note that, based on a large sample of low-redshift AGNs selected from the Swift/BAT, Rusinek et al. (2020) recently find a mean production efficiency of $\langle \eta_{\text{jet}} \rangle \approx 2 \times 10^{-5}$ ($\epsilon/10\%$). Part of the reason for such low $\langle \eta_{\text{jet}} \rangle$ is because that, about 80% of the sources in their sample are RQ AGNs, which by definition are systems with low η_{jet} .

Second, even within this limited (but near-complete) sample of Seyferts, a gradual decline in $\eta_{\text{jet}} f_X / \epsilon$ (and η_{jet}) as the system brightens (larger in L_X/L_{Edd}) is also observed. Considering the positive dependence on L_X/L_{Edd} in both f_X and ϵ (Vasudevan & Fabian 2009; Xie & Yuan 2012), this implies an efficient reduction in η_{jet} , or equivalently a jet quenching behavior, as L_X/L_{Edd} increases. As shown in Figure 5, the whole sample follows a negative relationship

$$\log(\eta_{\text{jet}} f_X / \epsilon) = -0.52^{+0.09}_{-0.09} \log(L_X/L_{\text{Edd}}) - 2.77^{+0.25}_{-0.25}. \quad (11)$$

For our adopted values of f_X and ϵ , it can also be expressed as

$$\log \eta_{\text{jet}} = -0.52^{+0.09}_{-0.09} \log(L_{\text{bol,h}}/L_{\text{Edd}}) - 4.45^{+0.15}_{-0.15}, \quad (12)$$

The results of Pearson correlation analysis are provided in Table 2. We note that such a negative correlation is also observed in literature (e.g., Wójtowicz et al. 2020). It is also consistent with the well-known anti-correlation between radio loudness and bolometric luminosity in AGNs (e.g., Terashima & Wilson 2003; Panessa et al. 2007; Ho 2008) and BHBs (Fender et al. 2009) as well.

For completeness, we include in Table 3 the estimations of the mean values of η_{jet} for different subsamples, i.e. Seyfert 1s vs. Seyfert 2s. There is no clear difference in η_{jet} among Sy 1s and Sy 2s. Moreover, although the η_{jet} of RL AGNs is about one order magnitude larger than that of RQ AGNs, it's still smaller than that reported in literature (e.g., Inoue et al. 2017; Wójtowicz et al. 2020).

Finally we caution that for RQ AGNs, not only the jet power estimation method is uncertain, there are also debates on the radio

Table 3. Jet Production Efficiency η_{jet} (and $\eta_{\text{jet}} f_X / \epsilon$) of *INTEGRAL*-Selected Seyferts

Sample (No.)	$\langle \eta_{\text{jet}} f_X / \epsilon \rangle$	$\langle \eta_{\text{jet}} \rangle$ ($f_X = 16$ and $\epsilon = 8\%$)
Full sample (64)	$3.8^{+1.7}_{-3.0} \times 10^{-2}$	$1.9^{+0.9}_{-1.5} \times 10^{-4}$
RQ (37)	$1.4^{+0.3}_{-0.8} \times 10^{-2}$	$6.9^{+1.7}_{-4.1} \times 10^{-5}$
RL (27)	$1.6^{+0.4}_{-0.9} \times 10^{-1}$	$7.9^{+1.9}_{-4.5} \times 10^{-4}$
Sy 1s (35)	$2.8^{+1.2}_{-2.2} \times 10^{-2}$	$1.4^{+0.6}_{-1.1} \times 10^{-4}$
Sy 2s (29)	$5.5^{+2.5}_{-4.3} \times 10^{-2}$	$2.8^{+1.3}_{-2.2} \times 10^{-4}$

origin. If other mechanisms play a dominant role, the jet production efficiency reported above will be an over-estimation.

4.3 BHBs versus AGNs

It is known that there are distinctive differences among bright AGNs and low-luminosity AGNs (e.g., Ho 2008 for a review), where the separation is around $L_{\text{bol}}/L_{\text{Edd}} \simeq (1 - 2)\%$ or $L_X/L_{\text{Edd}} \simeq 10^{-3}$. Direct connections or analogies between bright AGNs and BHBs in soft state (and possibly the intermediate state, see Belloni 2010 for state classification in BHBs), and between low-luminosity AGNs and BHBs in hard state, are now crudely established (among others, see e.g., Kórding, Jester, & Fender 2006; Ho 2008; Yuan & Narayan 2014; Yang et al. 2015). The accretion modes in the bright AGNs and low-luminosity AGNs correspond to, respectively, the two feedback modes established in AGN feedback field (Fabian 2012; Kormendy & Ho 2013; Heckman & Best 2014). The Seyfert galaxies in this work have an X-ray luminosity of $L_X \sim (10^{-4} - 1) L_{\text{Edd}}$, i.e. most of them belong to the bright AGN regime, thus may be powered by cold accretion disc (e.g., SSD, or the two-phase accretion flow, cf. Yang et al. 2015), and the rest are powered by hot accretion flow. We emphasize that the X-rays cannot be from the SSD, but may be from the corona above (and below) the SSD.

One unresolved puzzle in accretion theory is that, BHBs usually stay in their soft state when $L_X/L_{\text{Edd}} \gtrsim 10^{-3}$. In this state, the accretion is a cold SSD (Shakura & Sunyaev 1973), and the continuous jet will usually be quenched.¹¹ On the other hand, although the fraction of radio loudness declines as luminosity increases (e.g., Terashima & Wilson 2003; Ho 2008, and Sec. 4.2), a significant fraction (typically $\sim 10\%$) of bright AGNs still have detectable radio emission, some of which are even radio loud. Such discrepancy among BHBs and AGNs is fairly robust, but the corresponding physical reason remains unclear (see next section).

4.4 Jet production

Theoretically, the jet power is determined by the BH spin and the magnetic flux near BH (Blandford & Znajek 1977; Ghisellini et al. 2014; Tchekhovskoy 2015). However, in the discrepancy among BHBs and AGNs, the BH spin is known not to be a dominate factor. For example, even for BHBs whose BH spin is large (e.g., $a > 0.8$;

¹¹ We note that the compact jet in the soft state is also discovered recently in a limited number of systems and/or outbursts, e.g., Cyg X-3 (Zdziarski et al. 2018), GRS 1739–278 (Xie, Yan & Wu 2020), and Cyg X-1 (Zdziarski et al. 2020). These observations are of crucial importance, since they find in BHBs the counterparts of RL bright AGNs (and quasars).

Miller & Miller 2015), the jet is still quenched during soft state. Even for AGNs, it is known that many Seyferts with large BH spin are radio-quiet (Reynolds 2014), i.e. there is no direct link between BH spin and jet power.

The only possible mechanism left relates to the magnetic flux (or somewhat equivalently, the magnetic field strength) near BH. Indeed, theoretically Heinz & Sunyaev (2003) argued that there is a M_{BH} -dependence in the jet physics itself. In their scale invariant jet model, a larger M_{BH} leads to a relatively stronger magnetic field near the BH, which would make it easier to launch a relativistic jet. One possible prediction of this model is that, the jet velocity may be larger in a system with relatively stronger magnetic fields (i.e. larger in M_{BH}), where acceleration may be more efficient. Observationally there is indeed supporting evidence. In AGNs with supermassive BHs ($M_{\text{BH}} \sim 10^{7-9} M_{\odot}$) the jets are usually relativistic with $\Gamma \sim 10$ (Kellermann et al. 2004); in narrow-line Seyfert 1s ($M_{\text{BH}} \sim 10^6 M_{\odot}$), the jets are only mildly relativistic with $\Gamma \sim 3 - 5$ (Gu et al. 2015); and in the hard state of BHBs ($M_{\text{BH}} \sim 10 M_{\odot}$) the jet velocity is fairly low with $\Gamma \sim 1 - 2$ (Fender et al. 2009).

One important uncertainty in this picture is that, the central engine of bright AGNs as investigated here may be dominated by a cold SSD (thus most prominent in optical and UV radiation; while the X-ray emission is of secondary role), and it remains unclear whether or not a large-scale magnetic field can be developed around a cold disc like SSD. Recent high resolution magnetohydrodynamic simulations of SSDs reveal that, through the surface layer accretion process, the global vertical magnetic fields can be dragged inward and accumulate near BH. Consequently a magnetically-arrested disc (MAD) – capable of launching a relativistic jet – can then be achieved (e.g., Avara et al. 2016; Mishra et al. 2020). However, we emphasize that the dynamical structure of these simulations are highly different to those conventional weakly magnetized ones. Besides, it is unclear why some systems can enter into such an unusual state while the rest cannot. The observations of Seyfert galaxies report a fairly low η_{jet} ($\sim 10^{-4}$; see Figure 5 and Equation 12), which is much lower than that predicted by MAD (e.g., Ghisellini et al. 2014). In other words, it may suggest that the central engine of the hard X-ray selected Seyfert galaxies of P15 is magnetically “weak”, far away from the highly magnetized MAD state (a similar conclusion, see also Wójtowicz et al. 2020 for a sample of young radio galaxies). This is totally different from those γ -ray blazars as reported in Ghisellini et al. (2014), where a MAD state with nearly maximal possible jet power is observed.

4.5 Follow-ups and outlook

We note that, although the *INTEGRAL*/IBIS survey provides a complete sample of Seyfert galaxies from hard X-rays, it is not a deep/sensitive survey. The P15 sample includes only 79 sources. This limits our capabilities to explore fainter systems. One promising hard X-ray survey is done by the *Swift*/BAT (Koss et al. 2017), whose sensitivity is about one order of magnitude higher than the *INTEGRAL*/IBIS survey. Investigations based on the *Swift*/BAT sample will definitely be helpful to this problem (see e.g., Rusinek et al. 2020 for the investigation of η_{jet}). Most importantly, the *Swift*/BAT survey will enlarge the sample size of sources below 10^{-4} in $L_{\text{X}}/L_{\text{Edd}}$ and/or less massive in M_{BH} . The first is the regime which is more ideal to the standard so-called “radiatively-inefficient” hot accretion (Yuan & Narayan 2014), while the latter will (partially) fulfill the BH mass gap between BHBs and AGNs.

As mentioned in Sec. 4.1, to explore the possible physical models for the radio emission in RQ AGNs, high resolution and high

sensitivity radio observations are the keys to unravel the core region. Recently, Fischer et al. (2021) perform simultaneous radio (VLBA) and X-ray observations for 25 AGNs. Despite a low detection rate (36%) in radio, it allows us to explore the possible physical mechanism of RQs. They found AGNs in their sample jump out the FP from VLBA observations, but follow the FP from VLA observations, which implies that this discrepancy might be contributed by extranuclear radio emissions.

5 SUMMARY AND CONCLUSIONS

Sample selection/control is always an important issue in the fundamental plane investigation (e.g., Panessa et al. 2007; Li, Wu & Wang 2008; Xie & Yuan 2017; Yao et al. 2018). In this work, we focus on a complete hard X-ray selected sample of Seyfert galaxies originally gathered by P15. We only include sources that have measurements/estimations of BH mass and luminosities in radio and X-rays. Our final near-complete sample includes 64 (out of the original 79) sources, among which 35 are Seyfert 1s and 29 are Seyferts 2s, or 27 are RL and 37 are RQ. The dynamical range in $L_{\text{X}}/L_{\text{Edd}}$ is between $\sim 10^{-4}$ and $\sim 10^{-0.5}$. According to the typical separation of $L_{\text{X}}/L_{\text{Edd}} \sim 10^{-3}$ (e.g., Ho 2008; Yang et al. 2015), most sources of our sample belong to bright AGNs, and a small fraction are low-luminosity ones.

This near-complete hard X-ray selected sample suffers a strong dependence of $L_{\text{X}}/L_{\text{Edd}}$ on M_{BH} , as clearly shown in the left panel of Figure 1. We thus limit ourselves only to probe the radio/X-ray correlation in Eddington units (e.g., $L_{\text{R}}/L_{\text{Edd}}$ vs. $L_{\text{X}}/L_{\text{Edd}}$). This choice reflects our motivation to investigate the accretion theory, where only luminosities in Eddington units are related to the accretion mode (see Esin et al. 1997; Ho 2008; Yuan & Narayan 2014).

Our main results can be summarized as follows.

- There is no clear difference in $L_{\text{HX}}/L_{\text{X}}$ (mean value, scatter, distribution) among Seyfert 1s and Seyfert 2s, and among RL Seyferts and RQ Seyferts. This may suggest a common origin of X-rays in our sample.
- The slope of the radio/X-ray correlation is almost universal among different types of sources, i.e. it is irrelevant to the broad emission line properties (Seyfert 1s or 2s), the radio loudness (RL or RQ), and the morphological size of radio emission (extended or compact). The whole sample follows $L_{\text{R}}/L_{\text{Edd}} \propto (L_{\text{X}}/L_{\text{Edd}})^{0.77 \pm 0.10}$, which agrees with the standard FP at 2σ level (Merloni et al. 2003).
- Under the jet origin interpretation, the average jet production efficiency of Seyfert galaxies is $\langle \eta_{\text{jet}} \rangle = 1.9^{+0.9}_{-1.5} \times 10^{-4}$, which is two orders of magnitude lower than that of RL sources at even higher bolometric luminosities (van Velzen & Falcke 2013; Inoue et al. 2017; Soares & Nemmen 2020; Wójtowicz et al. 2020). More specifically, we have $\langle \eta_{\text{jet}} \rangle = 7.9^{+1.9}_{-4.5} \times 10^{-4}$ for RL Seyferts and $\langle \eta_{\text{jet}} \rangle = 6.9^{+1.7}_{-4.1} \times 10^{-5}$ for RQ Seyferts. Besides, a gradual decline in η_{jet} as the system brightens is also evident, i.e. $\eta_{\text{jet}} \propto (L_{\text{bol,h}}/L_{\text{Edd}})^{-0.52 \pm 0.09}$. Such jet quenching process during the brightening phase is expected in both theory and observations.

ACKNOWLEDGMENTS

We appreciate the referee for his/her detailed report and thoughtful comments (especially updates of radio emission in RQ systems) that improve our presentation. This work was supported by the National Key R&D Program of China (NKRDC, 2018YFA0404602), and

the Key Laboratory of Radio Astronomy, Chinese Academy of Sciences (CAS). FGX was supported in part by National SKA Project of China No. 2020SKA0110102, the National Science Foundation of China (NSFC, 11873074) and the Youth Innovation Promotion Association of CAS. LCH was supported by NKRDC (2016YFA0400702) and NSFC (11721303 and 11991052). This work has made extensive use of the NASA/IPAC Extragalactic Database (NED), which is operated by the Jet Propulsion Laboratory, California Institute of Technology, under contract with the NASA. This research has made use of the SIMBAD database, operated at CDS, Strasbourg, France.

REFERENCES

- Avara M. J., McKinney J. C., Reynolds C. S., 2016, *MNRAS*, 462, 636
- Baek J., Chung A., Schawinski K., Oh K., Wong O. I., Koss M., Ricci C., Trakhtenbrot B., Smith K. L., Ueda Y., 2019, *MNRAS*, 488, 4317
- Belloni T. M., 2010, *LNP*, 794, 53
- Blandford R. D., Meier D., Readhead A., 2019, *ARA&A*, 57, 467
- Blandford R. D., Znajek R. L., 1977, *MNRAS*, 179, 433
- Bonchi A., Franca F. La., Melini G., Bongiorno A., Fiore F., 2013, *MNRAS*, 429, 1970
- Bock D. C., Large M. I., Sadler E. M., 1999, *AJ*, 117, 1578
- Bourda G., Collioud A., Charlot P., Porcas R., Garrington S., 2011, *A&A*, 526, A102
- Burlon D., Ghirlanda G., Murphy T., Chhetri R., Sadler E., Ajello M., 2013, *MNRAS*, 431, 2471
- Cavagnolo K. W., McNamara B. R., Nulsen P. E. J., Carilli C. L., Jones C., Birzan L., 2010, *ApJ*, 720, 1066
- Chen L., Zhang B., 2020, *ApJ* (in press), arxiv: 2010.14470
- Chiaraluze E., Panessa F., Baldi R. D., Behar E., Vagnetti F., Tombesi F., McHardy I., 2020, *MNRAS*, 495, 3943
- Condon J. J., 1992, *ARA&A*, 30, 575
- Condon J. J., Conton W. D., Greisen E. W., Yin Q. F., Perley R. A., Taylor G. B., Broderick J. J., 1998, *AJ*, 115, 1693
- Condon J. J., Kellermann K. I., Kimball A. E., Ivezić Ž., Perley R. A., 2013, *ApJ*, 768, 37
- Corbel S., Nowak M. A., Fender R. P., Tzioumis A. K., Markoff S., 2003, *A&A*, 400, 1007
- Corbel S., Coriat M., Brocksopp C., Tzioumis K. T., Fender P. P., Tomsick J. A., Buxton M. M., Bailyn C. D., 2013, *MNRAS*, 428, 2500
- Coriat M., et al., 2011, *MNRAS*, 414, 677
- Croton D. J., et al., 2006, *MNRAS*, 365, 11
- de Gasperin F., Merloni A., Sell P., Best P., Heinz S., Kauffmann G., 2011, *MNRAS*, 415, 2910
- Davis S. W.; Tchekhovskoy A., 2020, *ARA&A*, 58, 407
- Dodson R., et al., 2008, *ApJS*, 175, 314
- Duan X., Guo F., 2020, *ApJ*, 896, 114
- Esin A. A., McClintock J. E., Narayan R., 1997, *ApJ*, 489, 865
- Fabian A. C., 2012, *ARA&A*, 50, 455
- Falcke H., Körding E., Markoff S., 2004, *A&A*, 414, 895
- Fanaroff B. L., Riley J. M., 1974, *MNRAS*, 167, 31
- Fender R. P., Homan J., Belloni T. M., 2009, *MNRAS*, 396, 1370
- Fischer, T. C., Secrest, N. J., Johnson, M. C., Dorland, B. N., Cigan, P. J., Fernandez, L. C., Hunt, L. R., Koss, M., Schmitt, H. R., Zacharias, N., 2021, *ApJ*, 906, 88
- Ghisellini G., Tavecchio F., Maraschi L., Celotti A., Sbarro T., 2014, *Nature*, 515, 376
- Giroletti M., Panessa F., 2009, *ApJ*, 706, L260
- Godfrey L. E. H., & Shabala S. S., 2013, *ApJ*, 767, 12
- Graham A. W., 2007, *MNRAS*, 379, 711
- Gu M., Chen Y., Komossa S., Yuan W., Shen Z., Wajima K., Zhou H., Zensus J. A., 2015, *ApJS*, 221, 3
- Guedel M., Benz A. O., 1993, *ApJ*, 405, L63
- Gültekin, K., Cackett E. M., Miller J. M., Matteo T. D., Markoff S., Richstone D. O., 2009, *ApJ*, 706, 404
- Gültekin, K., King A. L., Cackett E. M., Nyland K., Miller J. M., Matteo T. D., Markoff S., Rupen M. P., 2019, *ApJ*, 871, 80
- Hardcastle, M. J., Croston, J. H., 2020, *New Astron. Rev.*, 88
- Harris, D. E., Krawczynski H., 2006, *ARA&A*, 44, 463
- Heckman T. M., Best P. N., 2014, *ARA&A*, 52, 589
- Heinz S., Sunyaev R. A., 2003, *MNRAS*, 343, L59
- Ho L. C., 2008, *ARA&A*, 46, 475
- Ho L. C., 2009, *ApJ*, 699, 626
- Inoue Y., Doi A., Tanaka Y. T., Sikora M., Madejski G. M., 2017, *ApJ*, 840, 46
- Kauffmann G., Haehnelt M., 2000, *MNRAS*, 311, 576
- Kellermann K. I., Sramek R., Schmidt M., Shaffer D. B., Green R., 1989, *AJ*, 98, 1195
- Kellermann K. I., et al., 2004, *ApJ*, 609, 539
- Khorunzhev G. A., Sazonov S. Y., Burenin R. A., Tkachenko A. Y., 2012, *Astron. Lett.*, 38, 475
- Kim J.-Y., et al., 2019, *A&A*, 622, A196
- Kormendy J., Ho L. C., 2013, *ARA&A*, 51, 511
- Koss M., et al., 2017, *ApJ*, 850, 74
- Laor A., Behar E., 2008, *MNRAS*, 390, 847
- Laor A., Baldi, R. D., 2019, *MNRAS*, 482, 5513
- LaMassa S. M., et al., 2015, *ApJ*, 800, 144
- Li S.-L., Gu M., 2018, *MNRAS*, 481, L45
- Li S.-L., Xie F. G., 2017, *MNRAS*, 471, 2848
- Li Z.-Y., Wu X.-B., Wang R., 2008, *ApJ*, 688, 826
- Liao M., Gu M., Zhou M., Chen L., 2020, arXiv:2006.01079
- Liu X., Han Z. H., Zhang Z., 2016, *Ap&SS*, 361, id9
- Körding E. G., Jester S., Fender R., 2006, *MNRAS*, 372, 1366
- Malizia A., Stephen J. B., Bassani L., Bird A. J., Panessa F., Ubertini P., 2009, *MNRAS*, 399, 944
- Martini P., Weinberg D. H., 2001, *ApJ*, 547, 12
- McNamara B. R., Nulsen P. E. J., 2012, *NJPh*, 14, 055023
- Merloni A., Heinz S., di Matteo T., 2003, *MNRAS*, 345, 1057
- Merloni A., Heinz S., 2008, *MNRAS*, 388, 1011
- Middelberg E., Roy A. L., Nagar N. M., Krichbaum T. P., Norris R. P., Willson A. S., Falcke H., Colbert E. J. M., Witzel A., Fricke K. J., 2004, *A&A*, 417, 925
- Miller M. C., Miller J. M., 2015, *Phys. Rep.*, 548, 1
- Miller J. M., Reynolds C. S., Fabian A. C., Miniutti G., Gallo L. C., 2009, *ApJ*, 697, 900
- Mishra B., Begelman M. C., Armitage P. J., Simon J. B., 2020, *MNRAS*, 492, 1855
- Nagar N. M., Falcke H., Wilson A. S., 2005, *A&A*, 435, 521
- Netzer H., 2008, *New Astron. Rev.*, 52, 257
- Netzer H., 2015, *ARA&A*, 53, 365
- Netzer H., 2019, *MNRAS*, 488, 5185
- Orienti M., Prieto M. A., 2010, *MNRAS*, 401, 2599
- Qian L., Dong X.-B., Xie F. G., Liu W. J., Li, D., 2018, *ApJ*, 860, 134
- Padovani P., 2016, *A&ARv*, 24, 13
- Padovani P., Bonzini M., Kellermann K. I., Miller N., Mainieri V., Tozzi P., 2015, *MNRAS*, 452, 1263
- Padovani P., Alexander D. M., Assef R. J., De Marco B., Giommi P., Hickox R. C., Richards G. T., et al., 2017, *A&ARv*, 25, 2
- Panessa F., Barcons X., Bassani L., Cappi M., Carrera F. J., Ho, L. C., Pellegrini S., 2007, *A&A*, 467, 519
- Panessa F., Tarchi A., Castangia P., et al., 2015, *MNRAS*, 447, 1289 (P15)
- Panessa F., Bald R. D., Laor A., Padovani P., Behar E., McHardy I., 2019, *Nature Astronomy*, 3, 387
- Parfrey K., Philippov A., Cerutti B., 2019, *Phys. Rev. Lett.*, 122, 035101
- Raginski I., Laor A., 2016, *MNRAS*, 459, 2082
- Reynolds C. S., 2014, *Space Sci. Rev.*, 183, 277
- Rusinek K., Sikora M., Koziel-Wierzbowska D., Gupta M., 2020, *ApJ*, 900, 125
- Shabala S. S., Santoso J. S., Godfrey L. E. H., 2012, *ApJ*, 756, 161
- Shakura N. I., Sunyaev R. A. 1973, *A&A*, 24, 337
- Sikora M., Stawarz L., Lasota J.-P., 2007, *ApJ*, 658, 815
- Smith K. L., Mushotzky R. F., Koaa, M., Trakhtenbrot B., Ricci C. Wong

- O. I., Bauer F. E., Ricci F., Vogei S., Stern D., et al, 2020, MNRAS, 492, 4216
- Soares G., Nemmen R., 2020, MNRAS, 495, 981
- Struve C., Conway J. E., 2010, A&A, 513, A10
- Su, R. Z., Liu X., Zhang Z., 2017, Ap&SS, 362, 3
- Tehekhsvoiy A., 2015, in The Formation and Disruption of Black Hole Jets, eds. Contopoulos I., Gabuzda D., Kylafis N., Vol. 414 of Astrophysics and Space Science Library, Springer International Publishing, Switzerland, p. 45
- Terashima Y., Wilson A. S., 2003, ApJ, 583, 145
- Ulrich M.-H., Maraschi L., Urry C. M., 1997, ARA&A, 35, 445
- Ulvestad J. S., Antonucci R. R., Barvainis R., 2005, MNRAS, 621, 123
- Ünal C., Loeb A., 2020, MNRAS, 495, 278
- van Velzen S., Falcke H., 2013, A&A, 557, L7
- Vasudevan R. V., Fabian A. C., 2009, MNRAS, 392, 1124
- Wang R., Wu X.-B., Kong M.-Z., 2006, ApJ, 645, 890
- Willott C. J., Rawlings S., Blundell K. M., Lacy M., 1999, MNRAS 309, 1017
- Wójtowicz A., Stawarz Ł., Cheung C. C., Ostorero L., Kosmaczewski E., Siemiginowska A., 2020, ApJ, 892, 116
- Xie F. G., Yuan F., 2012, MNRAS, 427, 1580
- Xie F. G., Yuan F., 2016, MNRAS, 456, 4377
- Xie F. G., Yuan F., 2017, ApJ, 836, 104
- Xie F. G., Yan Z., Wu Z., 2020, ApJ, 891, 1
- Xie F. G., Zdziarski A. A., 2019, ApJ, 887, 167
- Yang Q. X., Xie F. G., Yuan F., Zdziarski A. A., Gierliński M., Ho L. C., Yu Z., 2015, MNRAS, 447, 1692
- Yao S., Qiao E., Wu X.-B., You B., 2018, MNRAS, 477, 1356
- Yuan F., Cui W., 2005, ApJ, 629, 408
- Yuan F., Cui W., Narayan R., 2005, ApJ, 620, 905
- Yuan F., Narayan R., 2014, ARA&A, 52, 529
- Zdziarski A. A., Malyshev D., Dubus G., et al., 2018, MNRAS, 479, 4399
- Zdziarski A. A., Shapopi J. N. S., Pooley G. G., 2020, ApJ 894, L18
- Zhuang, M.-Y., Ho, L. C., & Shangguan, J. 2021, ApJ, 906, 38

This paper has been typeset from a $\text{\TeX}/\text{\LaTeX}$ file prepared by the author.